metals

MDPI

Review

The Grain Boundary Wetting Phenomena in the Ti-Containing High-Entropy Alloys: A Review

Boris B. Straumal [1,2,*], Anna Korneva [3,*], Alexei Kuzmin [4], Gabriel A. Lopez [5], Eugen Rabkin [6], Alexander B. Straumal [1], Gregory Gerstein [7] and Alena S. Gornakova [1]

[1] Osipyan Institute of Solid State Physics of the Russian Academy of Sciences, Ac. Osipyan Str. 2, 142432 Chernogolovka, Russia; a.str@issp.ac.ru (A.B.S.); alenahas@issp.ac.ru (A.S.G.)
[2] Chernogolovka Scientific Center of the Russian Academy of Sciences, Lesnaja Str. 9, 142432 Chernogolovka, Russia
[3] Institute of Metallurgy and Materials Science, Polish Academy of Sciences, Reymonta St. 25, 30-059 Cracow, Poland
[4] Institute of Solid State Physics, University of Latvia, Kengaraga Str. 8, LV-1063 Riga, Latvia; a.kuzmin@cfi.lu.lv
[5] Physics Department, University of the Basque Country UPV/EHU, Barrio Sarriena s/n, 48940 Leioa, Spain; gabrielalejandro.lopez@ehu.es
[6] Department of Materials Science and Engineering, Technion—Israel Institute of Technology, Haifa 3200003, Israel; erabkin@technion.ac.il
[7] Institute of Materials Science, Leibnitz University of Hannover an der Universität 2, 30823 Garbsen, Germany; gerstein@iw.uni-hannover.de
* Correspondence: straumal@issp.ac.ru (B.B.S.); a.korniewa@imim.pl (A.K.); Tel.: +7-916-6768673 (B.B.S.)

Abstract: In this review, the phenomenon of grain boundary (GB) wetting by melt is analyzed for multicomponent alloys without principal components (also called high-entropy alloys or HEAs) containing titanium. GB wetting can be complete or partial. In the former case, the liquid phase forms the continuous layers between solid grains and completely separates them. In the latter case of partial GB wetting, the melt forms the chain of droplets in GBs, with certain non-zero contact angles. The GB wetting phenomenon can be observed in HEAs produced by all solidification-based technologies. GB leads to the appearance of novel GB tie lines T_{wmin} and T_{wmax} in the multicomponent HEA phase diagrams. The so-called grain-boundary engineering of HEAs permits the use of GB wetting to improve the HEAs' properties or, alternatively, its exclusion if the GB layers of a second phase are detrimental.

Keywords: titanium alloys; high-entropy alloys; grain boundary wetting; phase transitions; phase diagrams

Citation: Straumal, B.B.; Korneva, A.; Kuzmin, A.; Lopez, G.A.; Rabkin, E.; Straumal, A.B.; Gerstein, G.; Gornakova, A.S. The Grain Boundary Wetting Phenomena in the Ti-Containing High-Entropy Alloys: A Review. *Metals* **2021**, *11*, 1881. https://doi.org/10.3390/met11111881

Academic Editor: Andriy Ostapovets

Received: 30 October 2021
Accepted: 18 November 2021
Published: 22 November 2021

1. Introduction

According to the generally accepted definition, high-entropy alloys (HEAs) are materials that contain at least five different components, among which the main component cannot be selected [1–4]. Therefore, they are also called alloys without principal components or multiprincipal component alloys. High-entropy alloys have become extremely popular among researchers in recent years. There are literally thousands of articles devoted to them. For this reason, this review will be limited to two aspects. First, this review will consider alloys that contain titanium as principal or secondary component. Secondly, we will restrict ourselves to the phenomena associated with grain boundaries. Moreover, among the grain-boundary phenomena, emphasis will be placed on the phenomena associated with wetting-phase transformations.

High-entropy alloys containing titanium can be conventionally divided into two groups. The first group includes alloys containing zirconium and hafnium, together

with titanium [5–7]. Ti, Zr and Hf are in the same group in the Mendeleev periodic table of elements. Just like titanium, they have a body-centered crystal lattice at high temperatures (bcc, β-Ti, β-Zr, β-Hf), and at low temperatures, they possess a hexagonal close-packed lattice (hcp, α-Ti, α-Zr, α Hf). Moreover, at high pressure, all three metals transform into the high-pressure ω-phase with a more complex hexagonal lattice [8,9]. In some Ti-alloys, the metastable ω-phase appears even after certain heat treatment, without application of high pressure [10–12]. In HEAs containing titanium, zirconium and hafnium, other elements with a bcc lattice are most frequently present (for example, vanadium, molybdenum, tungsten, etc.). Therefore, such a HEAs will also have a body-centered cubic lattice. The second group is composed of alloys in which titanium plays a somewhat subordinate role [13–16]. In particular, these are the alloys with a face-centered cubic lattice (fcc) [17–21].

Generally speaking, from the very beginning of the studies of HEAs, it was noticed that in a certain range of compositions and temperatures, high-entropy alloys contain only one phase, namely a solid solution where all five or more components form a random solid solution [1–4]. Recently, the interest of researchers has shifted from such simple HEAs consisting of only one phase of a multicomponent solid solution to the alloys with certain elements of heterogeneity. These include the spatially inhomogeneous distribution of the components, the second-phase precipitates in a multicomponent solid solution, various grain-boundary layers, etc. For such studies, a special term, "metastability engineering", has been coined [22,23]. In many cases, the formation of such heterogeneous structures instead of a homogeneous multicomponent solid solution can be discussed in terms of phase transitions at grain boundaries (GBs). Such phase transformations include the wetting of grain boundaries with a melt or a second solid phase, as well as the formation of various thin grain-boundary layers of the second phase at the boundaries [24–27]. These phenomena depend non-trivially on the composition, temperature and pressure in a multicomponent system. This review is devoted to these grain-boundary processes in HEAs containing titanium.

2. Grain Boundary Wetting by the Liquid Phase

In the majority of cases, multicomponent alloys are synthesized by crystallization from the melt (arc or induction melting in vacuum or argon [5–7,13–18,28–43], plasma spark sintering [19], electric current assisted sintering [20,21], laser or plasma cladding deposition of coatings [44–55], additive manufacturing by the laser-powder bed fusion [56,57] or laser-metal deposition [58], self-propagating high-temperature synthesis (SHS) [59], and by brazing within the brazing joints [60,61]). Figure 1 shows a schematic phase diagram for the simplest case when there are only two components in the system. Cooling routes are shown by dashed lines 1 to 5 in Figure 1 for alloys with different compositions. Upon cooling, after crossing the liquidus line, the alloy first enters the two-phase region, where the melt, L, is in equilibrium with the solid solution, S. The melt solidifies completely when the temperature drops below the solidus line. We will use this schematic phase diagram in further explanations of GB phenomena. In the case of HEA, the situation is much more complicated. For example, six-component alloys are described by a phase diagram in six dimensions. In this case, between the single-phase melt, L, and the completely solidified material, S, there can be not one two-phase region, S + L, but many regions in which more than one solid and more than one liquid phase can coexist. If a polycrystalline sample is in the two-phase region, S + L, of the phase diagram, then it contains GBs in the solid phase and interphase boundaries between the solid phase and the melt. A triple junction of two interphase boundaries and one GB is formed in the locations where the GB is in contact with the melt (see Figure 1, schemes between Routes 1 and 2).

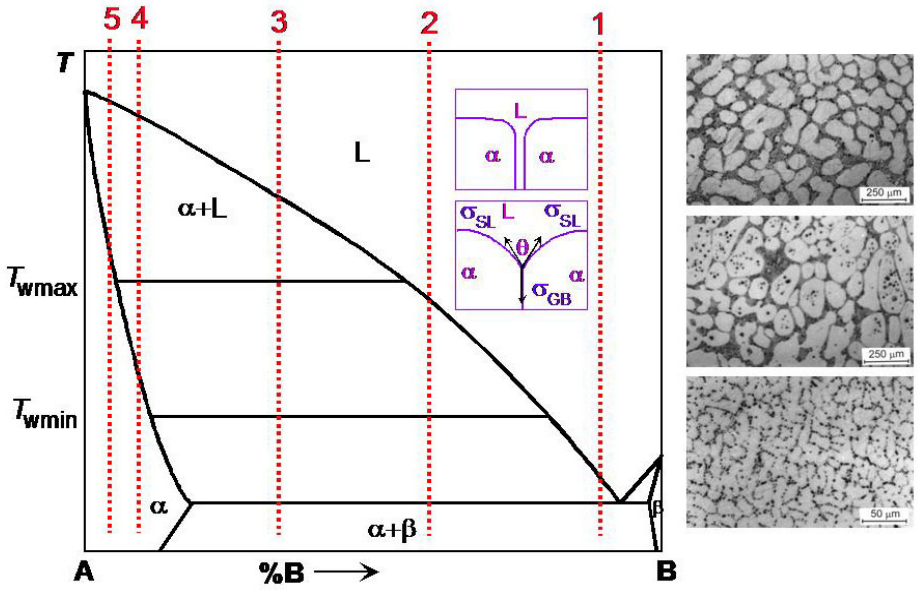

Figure 1. Schematic binary phase diagram for the explanation of GB wetting phenomena. Bold solid lines show the bulk-phase transformation. Thin solid lines show the tie lines of the GB wetting by the melt at T_{wmin} and T_{wmax}. Vertical red dotted lines 1 to 5 show different solidification routes. Schemes between Routes 1 and 2 show the cases of complete (top) and partial (bottom) GB wetting. Micrographs on the right-hand side of the diagram are for the Al-Mg samples annealed above T_{wmax} (top micrograph, all GBs are completely wetted), between T_{wmin} and T_{wmax} (middle micrograph, some GBs are completely wetted and other GBs are partially wetted) and below T_{wmin} (bottom micrograph, no completely wetted GBs).

If the energy of the GB σ_{GB} is less than the energy of the two solid/liquid interphase boundaries, $2\sigma_{SL}$, contacting this GB at the triple junction, then the contact angle, θ, at this triple junction is non-zero (see Figure 1). This situation with $\theta > 0$ is called incomplete (or partial) wetting of the GB by the melt. If the energy of the grain boundary is higher than the energy of the two solid/liquid interphase boundaries, $\sigma_{GB} > 2\sigma_{SL}$, then the contact angle will be equal to zero. In this case, the GB must be replaced by a sufficiently thick layer of the liquid phase. This situation is called complete wetting of the GB by the melt. In a number of systems, the angle between the GB and the melt decreases with increasing temperature [62–65]. Moreover, after reaching a certain temperature, T_w, the contact angle can become zero. In other words, incomplete wetting is replaced by complete wetting of the boundary. This temperature, T_w, is called the GB wetting phase-transition temperature. The wetting phase transition, like any other phase transformation, can be of either the first or the second order [66–68]. In the case of a first-order phase transition, the first derivative of the contact angle, with respect to temperature, exhibits a discontinuity at the temperature T_w [62,66,67]. It drops abruptly from a certain finite value to zero [62,66,67]. In the case of a second-order (continuous) phase transition, the first derivative of the contact angle with respect to temperature continuously decreases with increasing temperature and becomes equal to zero at the transformation temperature, T_w [66,67]. The energy of GBs depends on their misorientation angle, χ, and inclination angle, ψ [69]. It exhibits sharp cusps at certain χ and ψ values [70]. The energy spectrum of GBs can be very wide. Obviously, the higher the GB energy, the smaller the contact angle, θ, at its triple junction with the melt [71]. Thus, at a fixed temperature, a wide range of contact angles is observed in a two-phase polycrystal. As the temperature rises, these contact angles, θ, also decrease at different rates. This leads to the wide scatter of the GB wetting phase-transformation temperatures for the GBs with different energies.

The typical microstructures of such two-phase polycrystals are shown in Figure 1 for the binary Al–Mg alloys. Two tie lines for the transition from partial to complete wetting appear in the phase diagram. The first line at T_{wmin} corresponds to the GBs with the highest energy, σ_{GB}. Below this temperature, there are no completely wetted GBs in a polycrystal. It exhibits only partially wetted GBs with a nonzero contact angle, θ. Above the minimum wetting phase-transition temperature, T_{wmin}, the completely wetted GBs appear in the polycrystal. With a further increase in temperature, the fraction of such completely wetted boundaries in the sample increases until it reaches unity at T_{wmax}. This temperature, T_{wmax}, is indicated on the phase diagram by another horizontal tie line. Above this line, all grain boundaries are completely wetted (see diagram), and each grain is fully embedded in the melt without touching the other solid grains since the formation of "dry" GBs is thermodynamically unfavorable. Thus, in this region of the phase diagram, all solid crystallites are separated from each other by interlayers of the liquid phase. Consequently, in the phase diagram in the S + L two-phase region, where the solid and liquid phases are in equilibrium, the new tie lines appear. They are associated with GB wetting phase transformations. These lines are absent in traditional phase diagrams, which do not take into account the presence of grain boundaries in the sample. Accordingly, the microstructure of the polycrystal after solidification will be different for different solidification routes (see dotted lines 1 to 5). It will depend on the path along which the sample crosses the two-phase region during solidification. Such principally different situations for solidification are schematically shown in Figure 1 by vertical dotted lines 1 to 5.

The first dotted line, 1, on the right-hand side of Figure 1 does not intersect the grain boundary lines, T_{wmin} and T_{wmax}, in the phase diagram. When the melt is cooled, Route 1 crosses only the lines of bulk liquidus and the line of eutectic transformation. When such a sample solidifies, grain boundaries inside are formed immediately since they are not separated from each other by the liquid phase. The last pockets of the melt (the richest in the second component) are pushed into the triple junctions between the boundaries upon cooling and solidify there. This is the classical dendrite structure. Thus, after the solidification of such a melt, we can observe a relatively small difference in concentration between the centers of grains and the border regions, while the highest concentration of the second component is observed at the triple junctions of the GBs. As a result, the relatively homogeneous solid solution crystallizes, in which the enriched areas are well-visible. This scheme also works for multicomponent high-entropy alloys. Classical samples of single-phase high-entropy alloys, most likely, are just formed according to the scheme corresponding to the rightmost dotted line, 1. A typical sample of such a microstructure is shown in Figure 2 from Ref. [5]. When the melt is cooled, the second dashed line (Route 2) on the right-hand side of Figure 1 intersects not only the lines of the bulk liquidus and eutectic transformation but also the GB line at T_{wmin}. This means that the solid grains are separated from each other by liquid layers between the bulk liquidus and the grain-boundary tie line. Below the T_{wmin} tie line, these GB interlayers, enriched with the second component, solidify. Thus, enriched interlayers remain in the solid sample along these first GBs. Upon further cooling, the melt solidifies without the formation of grain-boundary-enriched interlayers. As dashed line 2 moves from right to left to Route 3, the sample will contain more and more GBs enriched with the second component after solidification. If the vertical dashed line (Route 3) also intersects the upper grain boundary tie line, T_{wmax}, then at the first stages of solidification, a continuous network of enriched interlayers is formed in the polycrystal between the solid grains (see the respective micrograph). It is subsequently clearly visible on the microstructure of the solidified alloy. At high concentrations of the second component, such a network has characteristic discontinuities (see, for example, the microstructure shown in Figure 3). The fourth vertical dashed line (Route 4) crosses only the bulk liquidus and tie line at T_{wmax}, and then the bulk solidus. In this case, thick enriched layers are visible at many GBs in the solidified sample. If the alloy does not cross the GB lines during cooling

(the fifth dotted line, Route 5), then the melt interlayers rich in the second component have no chance of redistributing in the solid state at all. They remain in the solidified sample in the form of a continuous network surrounding the grains poor in the second component (see, for example, the microstructure in Figure 4).

The scheme in Figure 1 is drawn for the simple binary systems. The real HEAs *per definitio* contain at least five components. This means that the respective HEAs' phase diagrams need five, six or more dimensions to be drawn. Moreover, according to the thermodynamic rule of phases, the multiphase areas containing different amounts of several solid and liquid phases should exist in the equilibrium phase diagrams for HEAs. This simple fact makes the description of GB wetting phenomena in HEAs much more complicated in comparison to binary systems. This review is a first attempt to discuss GB wetting in HEAs, to give the respective examples and draw the attention of readers to the open questions. We also hope to shed some light on possible causes of the formation of inhomogeneities in (traditionally homogeneous) HEAs.

3. GB Wetting in HEAs Obtained by the Arc or Induction Melting

The scheme shown in Figure 1 describes the most important scenarios of solidification in the presence of GB wetting phase transitions. However, in reality, the positions of T_{wmax} and T_{wmin} tie lines in relation to the melting temperature, T_m, and eutectic temperature, T_e, can be different. Let us consider some examples of HEA solidification. First, we discuss the crystallization from the melt during arc or induction melting in vacuum or argon [5–7,13–18,22–37]. If the two-phase S + L area of the phase diagram does not contain any tie lines, T_{wmax} or T_{wmin}, of the GB wetting transition, then the one-phase solid solution polycrystal with typical dendritic structure forms after solidification of the melt. This is the case of the equiatomic HfNbTaTiZr high-entropy alloy with bcc structure prepared by plasma arc melting (Figure 2a) [5]. After homogenization at 1473 K, this dendritic structure disappears and the bcc solid solution becomes homogenous (Figure 2b).

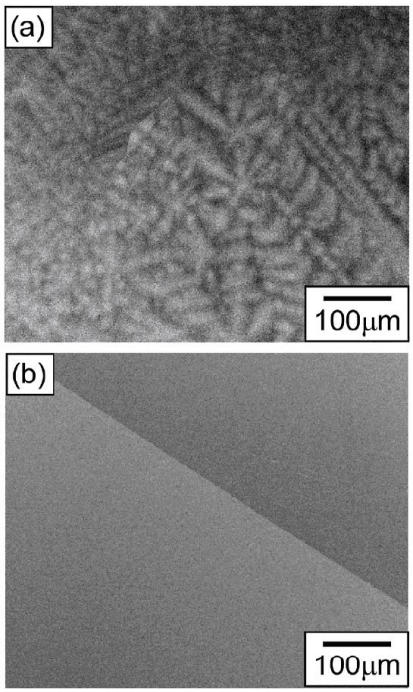

Figure 2. SEM micrographs of equiatomic HfNbTaTiZr polycrystal after arc melting, followed by homogenization treatment at 1773 K for 5 h; (**a**) as cast, (**b**) homogenized. Reprinted with permission from Ref. [5]. Copyright 2021 Elsevier.

Quite a different microstructure forms if the HEA solidifies following Route 3 or 4. In Figure 3, the SEM images of as-cast AlCoCuFeNiC (Figure 3a) and AlCoCuFeNiCrTi (Figure 3b) HEAs prepared by arc melting are shown [37]. The primary grains of the bcc phase were surrounded by the melt solidified as fcc phase. The majority of GBs were completely wetted by the melt. We describe the GB in a micrograph as completely wetted in the case when the melted layer is continuous from one GB triple junction (TJ) to another. If the melt layer between two TJs is broken and the portions of dry GB remain in between, we describe the GB as partially (incompletely) wetted. In this case, one can measure the non-zero contact angles in the contact points between the liquid phase and GB. However, some partially wetted GBs are also visible in micrographs in Figure 3. A similar microstructure was observed in the as-cast $Al_{0.5}$CoCuNiTi alloy prepared by arc melting [14]. In the as-cast state, the $Al_{0.5}$CoCuNiTi alloy is composed of the fcc matrix grains separated by the 1–4 μm thick layers of the bcc phase. It is also well visible from the micrographs in Ref. [14] that not all GBs were completely wetted by the liquid phase. Some of the GBs remained incompletely wetted with a non-zero contact angle.

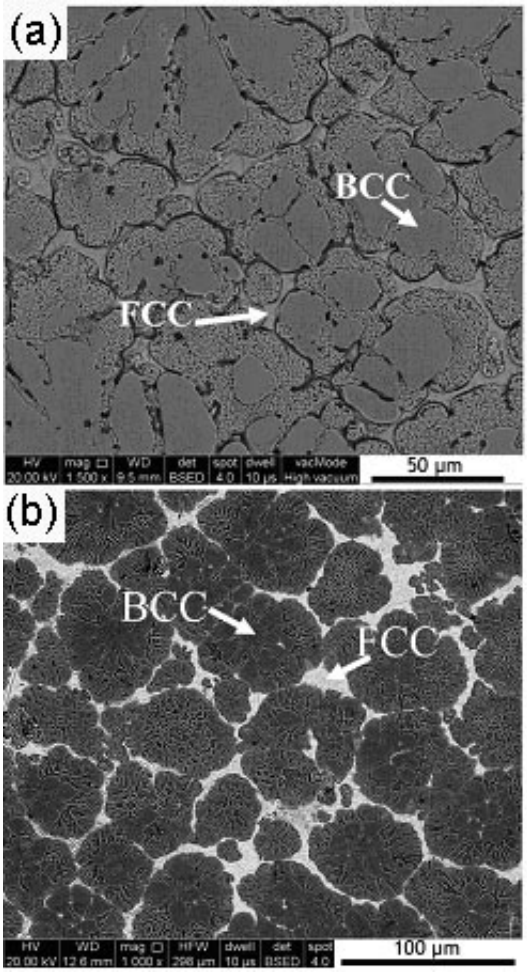

Figure 3. SEM micrographs of as-cast HEAs AlCoCuFeNiC (**e**) and AlCoCuFeNiCrTi (**g**). Reprinted with permission from Ref. [37]. Copyright 2017 Elsevier.

The change in HEA composition can modify the position of GB wetting T_{wmax} and T_{wmin} tie lines and, therefore, also the solidification route. Thus, in Ref. [28], two equiatomic AlCrCuFeTi and AlCrCuFeV HEAs were prepared by arc melting in a titanium-getter argon atmosphere. After solidification, the HEA consist of a bcc matrix with pronounced GB layers from other phase(s) (Figure 4 in [28]). These GB phases formed

after solidification of the last (intergranular) fractions of the melt. They are Cu-rich and are fcc in AlCrCuFeV alloy and bcc-2, with $L1_2$ Heussler and hexagonal Laves phases in the AlCrCuFeTi alloy. It is visible in Figure 4 in [28] that in the V-containing HEA, the fraction of completely wetted GBs is much higher (though even not 100%) than in the Ti-containing HEA (where it is 10–20%). This means that AlCrCuFeTi HEA solidified following Route 2 and AlCrCuFeV alloy solidified following Route 3 or 4 (see scheme in Figure 1).

A good example of complete GB wetting can be seen in the $Ti_3V_2NbNi_{0.5}$ alloy produced by the vacuum arc melting with multiple remelting passes (Figure 4) [13]. XRD, TEM and SAED data show that the matrix grains have disordered bcc structure, while the GB precipitates have cubic $MgCu_2$-type (C15) structure (so-called Laves phase). Here, the bcc solid crystallites were completely surrounded by the melt. Further, the last fractions of the melt eutectically decomposed into a bcc+ C15 mixture of solid phases.

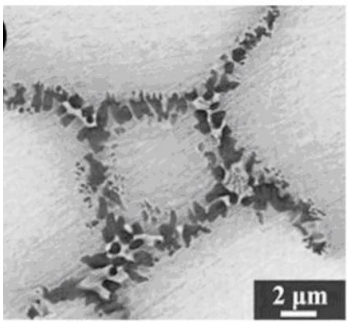

Figure 4. SEM BSE micrograph of the as-cast $Ti_3V_2NbNi_{0.5}$ alloy. The matrix grains are surrounded by the eutectic bcc+ C15 mixture. Reprinted with permission from Ref. [13]. Copyright 2021 Elsevier.

Another example of concentration dependence of solidification route in the presence of GB wetting tie lines can be found in the Ti-free CoCrFeNi-Ta_x HEAs with different concentration of Ta (x = 0.1, 0.25, 0.75, 1) [29]. HEAs were prepared by arc melting under argon atmosphere. The first two HEAs are hypoeutectic, and last two are hypereutectic (see phase diagram in Figure 5). In first two HEAs, the matrix has fcc structure, and GB layers contain the Laves phase formed after solidification. Figure 6a,b demonstrate that CoCrFeNi-$Ta_{0.1}$ HEA solidifies according to Route 2 (few completely wetted GBs), and the CoCrFeNi-$Ta_{0.25}$ HEA solidifies following Route 4 (nearly all GBs are wetted). In hypereutectic CoCrFeNi-$Ta_{0.75}$ and CoCrFeNi-$Ta_{1.00}$ HEAs, the situation is more complicated, but the GB wetting phenomena are, nevertheless, obvious (Figure 6c,d).

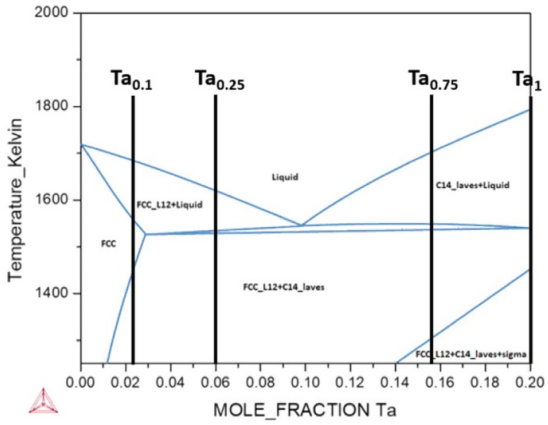

Figure 5. Pseudo-binary phase diagram of CoCrFeNi-Ta. Reprinted with permission from Ref. [29]. Copyright 2021 Elsevier.

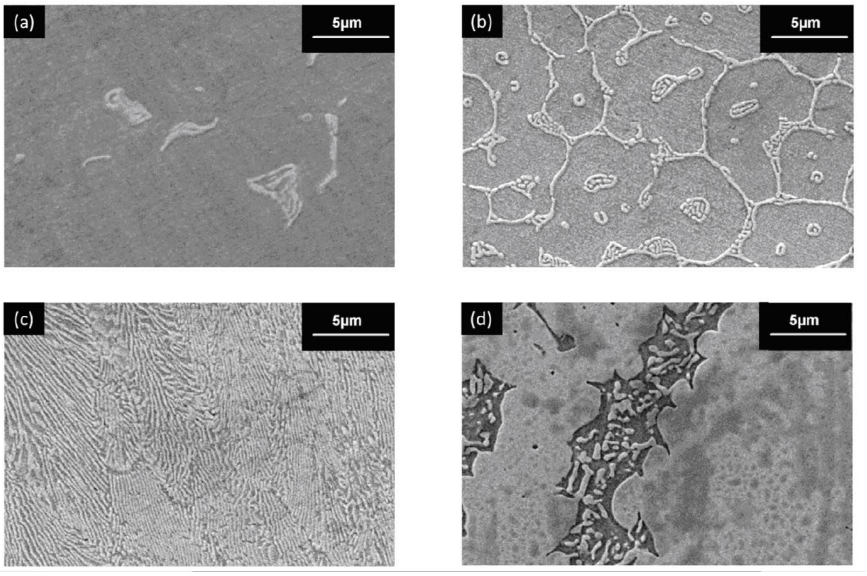

Figure 6. SEM micrographs of CoCrFeNi-Ta$_x$ HEA. (**a**) x = 0.1, (**b**) x = 0.25, (**c**) x = 0.75, (**d**) x = 1. Reprinted with permission from Ref. [29]. Copyright 2021 Elsevier.

4. GB Wetting in HEAs Obtained by Electric-Current-Assisted Sintering

In HEAs produced by methods other than arc melting, one can also observe the indications of GB wetting transitions. In Ref. [20], CoCrFeNi, CoCrFeNi $Ti_{0.5}Al_{0.5}$ and CoCrFeNi$Al_{0.5}$ high-entropy alloys were produced using electric-current-assisted sintering (ECAS). After the production of HEAs, they were laser remelted (LR). The CoCrFeNi alloy contained only one fcc phase and was completely uniform after LR (Figure 7a). Its solidification corresponds, therefore, to Route 1 (Figure 1). In the CoCrFeNi$Al_{0.5}$ and CoCrFeNi $Ti_{0.5}Al_{0.5}$ HEAs, however, the GBs of the bcc grains were completely wetted by the melt (Route 1 or 2). After solidification, the GB layers contained the second bcc phase rich in Cr (Figure 7b,c). This result also demonstrates that slight modification of the composition one can strongly change the morphology of phases by shifting the position of GB wetting tie lines, T_{wmax} and T_{wmin}, or (alternatively) the position of the solidification route when the temperatures, T_{wmax} and T_{wmin}, are fixed.

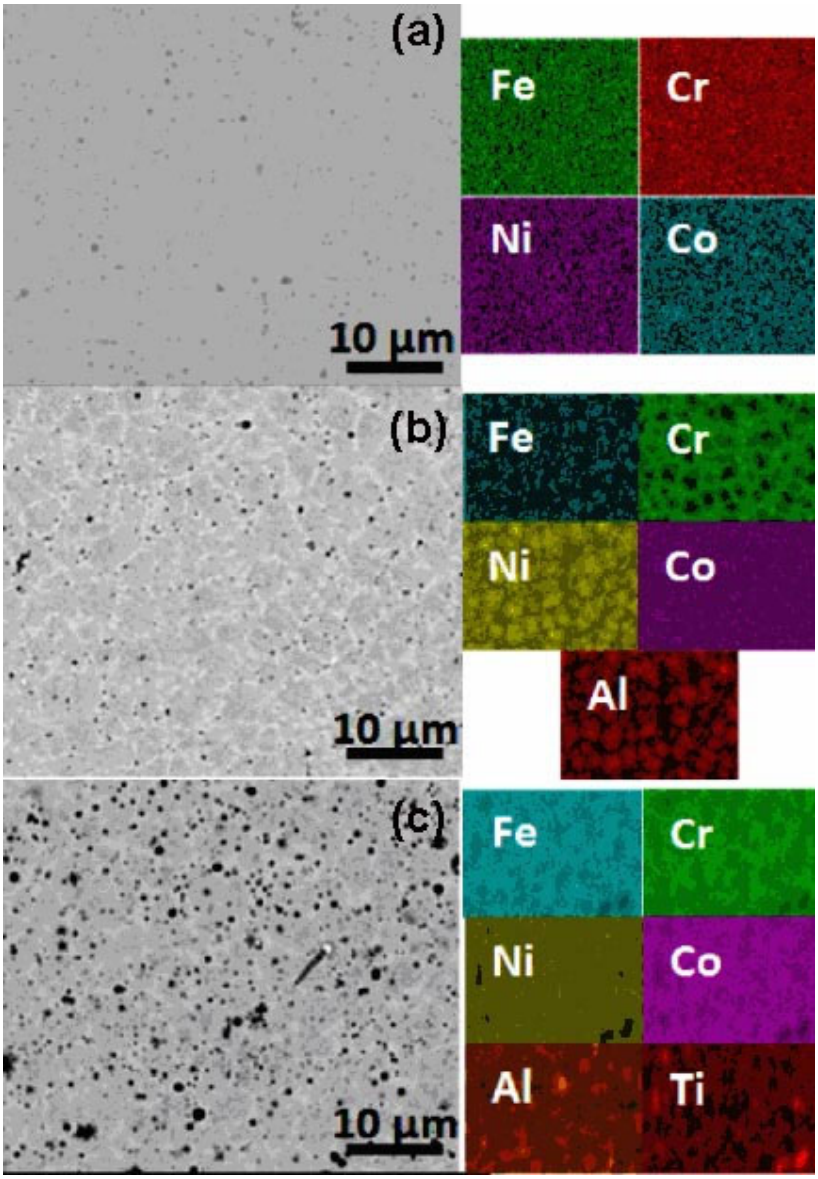

Figure 7. SEM-EDX-mapping analysis of sintered and laser-remelted HEAs: (**a**) CoCrFeNi, (**b**) $CoCrFeNiAl_{0.5}$, (**c**) $CoCrFeNiTi_{0.5}Al_{0.5}$. Reprinted with permission from Ref. [20]. Copyright 2021 Elsevier.

5. GB Wetting in HEAs Obtained by Laser Cladding and Additive Manufacturing

In Ref. [45], $MgMoNbFeTi_2Y_x$ (x = 0, 0.4%, 0.8%, 1.2%) HEA coatings were synthesized by laser cladding. After crystallization, they contain the matrix grains of the bcc-phase rich in Mo and Ni surrounded by the layers of Mg, Ti-rich phase (Figure 8). Almost all bcc grains are separated from each other by the Mg, Ti-rich 200–300 nm thick layers. Only a few GBs were partially wetted by the melt. This corresponds to solidification Routes 5 or 4 (Figure 1).

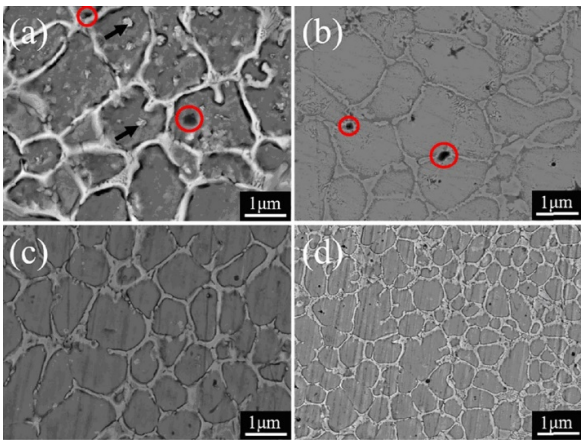

Figure 8. SEM micrographs of $MgMoNbFeTi_2Y_x$ HEA coatings (**a**) $x = 0$, (**b**) $x = 0.4\%$, (**c**) $x = 0.8\%$, (**d**) $x = 1.2\%$ deposited by laser cladding. Reprinted with permission from Ref. [45]. Copyright 2021 Elsevier.

In Ref. [46], $Al_xMo_{0.5}NbFeTiMn$ (x = 1, 1.5, 2) HEA coatings were synthesized by laser cladding. Their microstructure consists of an Mo,Ni-rich bcc-phase (matrix grains) surrounded by the layers of Mg,Ti-rich phase (Figure 9), similar to the alloys studied in Ref. [45]. It is interesting that the amount of former liquid phase (crystallized then as Mg,Ti-rich phase) increases with increasing concentration of aluminum (Figure 9a–c). It is important to underline that in Figure 9a,b some GBs are visible that are incompletely wetted by the melt (with non-zero contact angle). In Figure 9c, however, all GBs are completely wetted, and thick layers of the Mg,Ti-rich phase separate all grains of the Mo,Ni-rich bcc-phase from one another. The reason for that could be the so-called apparently complete GB wetting [72]. In case of apparently complete GB wetting, also GBs with a low but non-zero contact angle can also become completely replaced by the melt just because the wedges of the liquid phase from neighboring GB triple junctions meet each other and thus separate the solid grains.

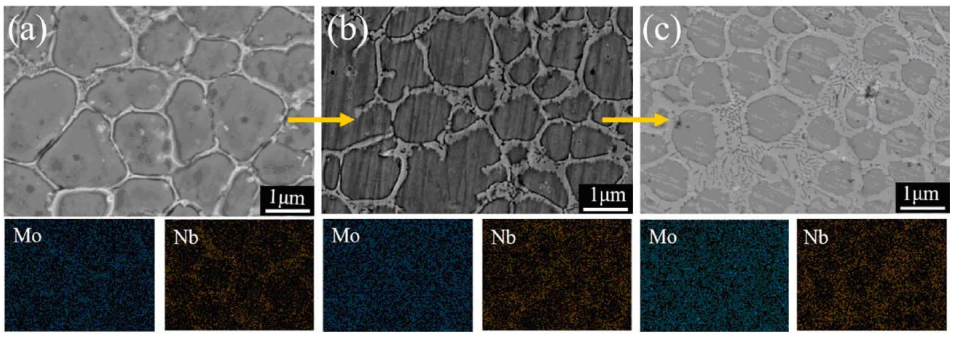

Figure 9. SEM micrographs of $Al_xMo_{0.5}NbFeTiMn$ HEAs deposited by laser cladding. (**a**) $x = 1$, (**b**) $x = 1.5$, (**c**) $x = 2$. The corresponding EDS maps for Nb and Mo are given in the bottom part. Reprinted with permission from Ref. [46]. Copyright 2020 Elsevier.

In Ref. [58], $AlCoCrFeNiTi_{0.5}$ HEA was prepared by the additive manufacturing method, namely laser metal deposition (LMD). The resulting microstructure consists of Al-, Ni-, Ti- and Co-rich grains (with fully ordered bcc structure B2), which are completely surrounded during solidification by the melt (see Figure 10). The melt later crystallized in the Cr- and Fe-rich solid phase with disordered bcc structure A2. It has been observed that changing the LMD regimes one can switch from a structure with equiaxial B2 grains surrounded by thick A2 layers (Figure 10) to a conventional dendrite structure similar to that shown in Figure 2a.

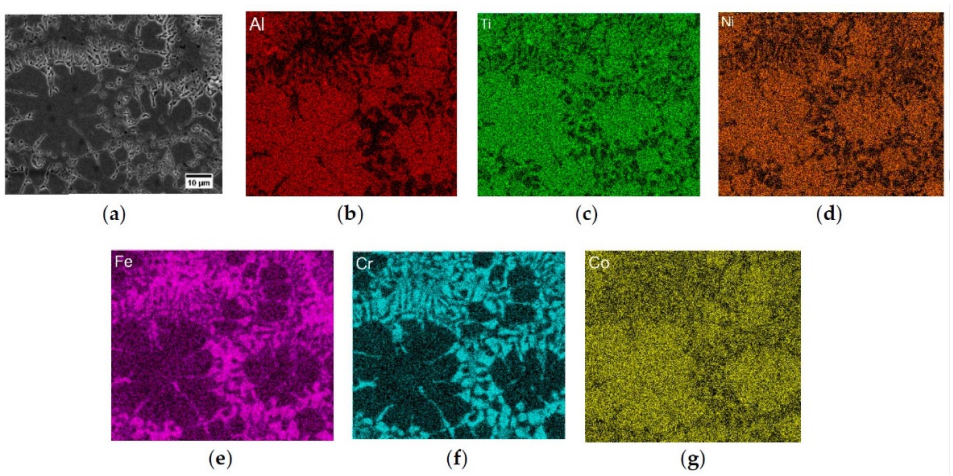

Figure 10. (**a**) Secondary electron image and the corresponding elemental maps of (**b**) Al, (**c**) Ti, (**d**) Ni, (**e**) Fe, (**f**) Cr and (**g**) Co of the $AlCoCrFeNiTi_{0.5}$ HEA. Reprinted with permission from Ref. [58]. Copyright 2020 MDPI.

In this review, we presented several examples of complete and partial GB wetting in solidified HEAs. These examples do not exhaust the cases of GB wetting in HEAs. They are just typical cases from recent publications. Indeed, similar microstructures can be frequently seen in publications devoted to HEAs.

As we can see, modern HEAs frequently contain more than just one random solid solution phase. Moreover, the morphology of minor phase(s), especially their distribution between the grains of major phases, can be governed by the GB wetting phenomena. These phenomena are well studied for the binary metallic alloys [73–78], and the respective knowledge can be successfully applied to multicomponent HEAs. In particular, in the two-phase S + L area(s) of a multicomponent phase diagram, the additional tie lines of the GB wetting phase transition can appear (at minimum T_{wmin} and maximum T_{wmax} temperatures). As a result, the minor melt phase (which later crystallizes) can form rather thick (at least few μm) layers separating the grains of major phases. The influence of such layers on HEA properties can be both favorable or detrimental. Knowledge of GB wetting transformations in HEAs can be used for tailoring their properties, as well as for the further development of these advanced materials.

6. Conclusions

The thick (at least few μm) grain-boundary layers of the second phase(s) can appear in HEAs during crystallization of the melt in all synthesis technologies (such as arc or induction melting, plasma-spark or electric-current-assisted sintering, deposition of coatings by laser or plasma cladding, additive manufacturing, self-heating synthesis or even in brazing applications). These thick GB layers are liquid during cooling in the S+L area of the HEA phase diagram and then crystallize as a second solid phase or decompose in eutectic or peritectic reactions. The formation of such thick GB layers is due to the phenomenon of complete or partial GB wetting. Thus, the equilibrium liquid layers between solid grains appear if the GB energy is higher than the energy of two solid-liquid interfaces. The presence of GB layers of a second phase(s) can have either a positive or a negative effect on the properties of HEAs. In any case, one can use the GB wetting phenomena to tailor the microstructure and properties of HEAs. For such so-called grain-boundary engineering of HEAs, knowledge of the position of GB wetting tie lines in the S + L areas of HEA phase diagrams is required.

Author Contributions: Conceptualization, B.B.S., A.S., A.G. and A.K.; methodology, A.K., A.K., G.A.L. and E.R.; formal analysis, A.K., A.K., G.A.L. and E.R.; writing—original draft preparation, A.K., A.K., G.A.L., A.S. and E.R.; writing—review and editing, B.B.S., A.G.; supervision, B.B.S., G.G. and A.K.; project administration, B.B.S., G.G. and A.K.; funding acquisition, B.B.S. and A.K. All authors have read and agreed to the published version of the manuscript.

Funding: This research was funded by the Russian Ministry Of Science And Higher Education (contract no. 075-15-2021-945 grant no. 13.2251.21.0013). Support from the University of the Basque Country under the GIU19/019 project is also acknowledged.

Institutional Review Board Statement: Not applicable.

Informed Consent Statement: Not applicable.

Data Availability Statement: Data are contained within the article or supplementary material.

Acknowledgments: This review is written during the preparation of M-era.Net full proposal "Grain boundaries in multicomponent alloys without principal component" (A.K., A.K., G.A.L. and E.R., application No. 9345). The Institute of Solid State Physics, University of Latvia, as a center of excellence, has received funding from the European Union's Horizon 2020 Framework Programme H2020-WIDESPREAD-01-2016-2017-TeamingPhase2 under grant agreement no. 739508, project CAMART².

Conflicts of Interest: The authors declare no conflicts of interest. The funders had no role in the design of the study; in the collection, analyses or interpretation of data; in the writing of the manuscript or in the decision to publish the results.

References

1. Cantor, B.; Chang, I.T.H.; Knight, P.; Vincent, A.J.B. Microstructural development in equiatomic multicomponent alloys. *Mater. Sci. Eng. A* **2004**, *375–377*, 213–218, https://doi.org/10.1016/j.msea.2003.10.257.
2. Yeh, J.W.; Chen, S.K.; Lin, S.J.; Gan, J.Y.; Chin, T.S.; Shun, T.T.; Tsau, C.H.; Chang, S.Y. Nanostructured high-Entropy alloys with multiple principal elements: Novel alloy design concepts and outcomes. *Adv. Eng. Mater.* **2004**, *6*, 299–303, https://doi.org/10.1002/adem.200300567.
3. Senkov, O.N.; Wilks, G.B.; Miracle, D.B.; Chuang, C.P.; Liaw, P.K. Refractory high-Entropy alloys. *Intermetallics* **2010**, *18*, 1758–1765, https://doi.org/10.1016/j.intermet.2010.05.014.
4. Senkov, O.N.; Isheim, D.; Seidman, D.N.; Pilchak, A.L. Development of a refractory high entropy superalloy. *Entropy* **2016**, *18*, 102, https://doi.org/10.3390/e18030102.
5. Yasuda, H.Y.; Yamada, Y.; Cho, K.; Nagase, T. Deformation behavior of HfNbTaTiZr high entropy alloy singe crystals and polycrystals. *Mater. Sci. Eng. A* **2021**, *809*, 140983, https://doi.org/10.1016/j.msea.2021.140983.
6. Nagase, T.; Iijima, Y.; Matsugaki, A.; Ameyama, K.; Nakano, T. Design and fabrication of Ti–Zr-Hf-Cr-Mo and Ti–Zr-Hf-Co-Cr-Mo high entropy alloys as metallic biomaterials. *Mater. Sci. Eng. C* **2020**, *107*, 110322, https://doi.org/10.1016/j.msec.2019.110322.
7. Eleti, R.R.; Chokshi, A.H.; Shibata, A.; Tsuji, N. Unique high-Temperature deformation dominated by grain boundary sliding in heterogeneous necklace structure formed by dynamic recrystallization in HfNbTaTiZr BCC refractory high entropy alloy. *Acta Mater.* **2020**, *183*, 64–77, https://doi.org/10.1016/j.actamat.2019.11.001.
8. Gupta, S.C.; Joshi, K.D.; Banerjee, S. Experimental and theoretical investigations on *d* and *f* electron systems under high pressure. *Metall. Mater. Trans. A* **2008**, *39*, 1593–1601, https://doi.org/10.1007/s11661-007-9377.
9. Hennig, R.; Trinkle, D.R.; Bouchet, J.; Srinivasan, S.G.; Albers, R.C.; Wilkins, J.W. Impurities block the alpha to omega martensitic transformation in titanium. *Nat. Mater.* **2005**, *4*, 129–133, https://doi.org/10.1038/nmat1292.
10. Sikka, S.K.; Vohra, Y.K.; Chidambaram, R. Omega-Phase in materials. *Prog. Mater. Sci.* **1982**, *27*, 245–310, https://doi.org/10.1016/0079-6425(82)90002-0.
11. Banerjee, S.; Mukhopadhyay, P. *Phase Transformations: Examples from Titanium and Zirconium Alloy*; Elsevier: Amsterdam, The Netherlands, 2010.
12. Hickman, B.S. The formation of omega phase in Ti and Zr alloys: A review. *J. Mater. Sci.* **1969**, *4*, 554–563, https://doi.org/10.1007/BF00550217.
13. Yao, H.; Liu, Y.; Sun, X.; Lu, Y.; Wang, T.; Li, T. Microstructure and mechanical properties of $Ti_3V_2NbAl_xNi_y$ low-Density refractory multielement alloys. *Intermetallics* **2021**, *133*, 107187, https://doi.org/10.1016/j.intermet.2021.107187.
14. Yi, J.; Wang, L.; Tang, S.; Yang, L.; Xu, M.; Liu, L. Microstructure and mechanical properties of $Al_{0.5}$CoCuNiTi high entropy alloy. *Phil. Mag.* **2021**, *101*, 1176–1187, https://doi.org/10.1080/14786435.2021.1886366.
15. Yi, J.; Tang, S.; Zhang, C.; Xu, M.; Yang, L.; Wang, L.; Zeng, L. Microstructure and mechanical properties of a new refractory equiatomic CrHfNbTaTi high-Entropy alloy. *JOM* **2021**, *73*, 934–940, https://doi.org/10.1007/s11837-020-04557-y.

16. Nong, Z.; Wang, H.; Wang, D.; Zhu, J. Investigation on structural stability of as-Cast $Al_{0.5}$CrCuFeMnTi high entropy alloy. *Vacuum* **2020**, *182*, 109686, https://doi.org/10.1016/j.vacuum.2020.109686.
17. Du, X.H.; Huo, X.F.; Chang, H.T.; Li, W.P.; Duan, G.S.; Huang, J.C.; Wu, B.L.; Zou, N.F.; Zhang, L. Superior strength-Ductility combination of a Co-Rich CoCrNiAlTi high entropy alloy at room and cryogenic temperatures. *Mater. Res. Express* **2020**, *7*, 034001, https://doi.org/10.1088/2053-1591/ab7a64.
18. Hernández-Negrete, O.; Tsakiropoulos, P. On the microstructure and isothermal oxidation at 800 and 1200 °C of the Nb–24Ti–18Si–5Al–5Cr–5Ge–5Sn (at.%) silicide-Dased alloy. *Materials* **2020**, *13*, 722, https://doi.org/10.3390/ma13030722.
19. Eißmann, N.; Mühle, U.; Gaitzsch, U.; Walther, G.; Weißgärber, T.; Kieback, B. Precipitation hardening of high entropy alloy CoCrFeMnNi containing titanium. *J. Alloys Compd.* **2021**, *857*, 157610, https://doi.org/10.1016/j.jallcom.2020.157610.
20. Döleker, K.M.; Erdogan, A.; Zeytin, S. Laser re-Melting influence on isothermal oxidation behavior of electric current assisted sintered CoCrFeNi, CoCrFeNi$Al_{0.5}$ and CoCrFeNi$Ti_{0.5}Al_{0.5}$ high entropy alloys. *Surf. Coat. Technol.* **2021**, *407*, 126775, https://doi.org/10.1016/j.surfcoat.2020.126775.
21. Erdogan, A.; Döleker, K.M.; Zeytin, S. Effect of laser re-Melting on electric current assistive sintered CoCrFeNiAl_xTi_y high entropy alloys: Formation, micro-hardness and wear behaviors. *Surf. Coat. Technol.* **2020**, *399*, 126179, https://doi.org/10.1016/j.surfcoat.2020.126179.
22. Jung, Y.; Lee, K.; Hong, S.J.; Lee, J.K.; Han, J.; Kim, K.B.; Liaw, P.K.; Lee, C.; Song, G.Investigation of phase-transformation path in TiZrHf(VNbTa)x refractory high-Entropy alloys and its effect on mechanical property. *J. Alloys Compd.* **2021**, *886*, 161187, https://doi.org/10.1016/j.jallcom.2021.161187.
23. Sun, F.; Zhang, J.Y.; Marteleur, M.; Brozek, C.; Rauch, E.F.; Veron, M.; Vermaut, P.; Jacques, P.J.; Prima, F. A new titanium alloy with a combination of high strength, high strain hardening and improved ductility. *Scripta Mater.* **2015**, *94*, 17–20, https://doi.org/10.1016/j.scriptamat.2014.09.00.
24. Chang, L.-S.; Straumal, B.B.; Rabkin, E.; Gust, W.; Sommer, F. The solidus line of the Cu–Bi phase diagram. *J. Phase Equil.* **1997**, *18*, 128–135, https://doi.org/10.1007/s11669-006-5002-z.
25. Chang, L.-S.; Rabkin, E.; Straumal, B.; Lejcek, P.; Hofmann, S.; Gust, W. Temperature dependence of the grain boundary segregation of Bi in Cu polycrystals. *Scripta Mater.* **1997**, *37*, 729–735, https://doi.org/10.1016/S1359-6462(97)00171-1.
26. Chang, L.-S.; Rabkin, E.; Straumal, B.B.; Hoffmann, S.; Baretzky, B.; Gust, W. Grain boundary segregation in the Cu–Bi system. *Defect Diff. Forum* **1998**, *156*, 135–146, https://doi.org/10.4028/www.scientific.net/DDF.156.135.
27. Schölhammer, J.; Baretzky, B.; Gust, W.; Mittemeijer, E.; Straumal, B. Grain boundary grooving as an indicator of grain boundary phase transformations. *Interf. Sci.* **2001**, *9*, 43–53, https://doi.org/10.1023/A:1011266729152.
28. Yi, J.; Wang, L.; Xu, M.; Yang, L. Two new 3d transition metals AlCrCuFeTi and AlCrCuFeV high-Entropy alloys: Phase components, microstructures, and compressive properties. *Appl. Phys. A* **2021**, *127*, 74, https://doi.org/10.1007/s00339-020-04212-y.
29. Mukarram, M.; Mujahid, M.; Yaqoob, K. Design and development of CoCrFeNiTa eutectic high entropy alloys. *J. Mater. Res. Technol.* **2021**, *10*, 1243–1249, https://doi.org/10.1016/j.jmrt.2020.12.042.
30. Guo, Z.; Liu, R.; Wang, C.T.; He, Y.; He, Y.; Ma, Y.; Hu, X. Compressive Mechanical properties and shock-Induced reaction behavior of a Ti–29Nb–13Ta–4.6Zr alloy. *Met. Mater. Int.* **2020**, *26*, 1498–1505, https://doi.org/10.1007/s12540-019-00414-z.
31. Yuefei Jia, Y.; Zhang, L.; Li, P.; Ma, X.; Xu, L.; Wu, S.; Jia, Y.; Wang, G. Microstructure and mechanical properties of Nb–Ti–V–Zr refractory medium-entropy alloys. *Front. Mater.* **2020**, *7*, 172, https://doi.org/10.3389/fmats.2020.00172.
32. Petroglou, D.; Poulia, A.; Mathiou, C.; Georgatis, E.; Karantzalis, A.E. A further examination of MoTa_xNbVTi (x = 0.25, 0.50, 0.75 and 1.00 at.%) high-Entropy alloy system: Microstructure, mechanical behavior and surface degradation phenomena. *Appl. Phys. A* **2020**, *126*, 364, https://doi.org/10.1007/s00339-020-03566-7.
33. Zhao, J.; Utton, C.; Tsakiropoulos, P. On the microstructure and properties of Nb-12Ti-18Si-6Ta-2.5W-1Hf (at %) silicide-Based alloys with Ge and Sn additions. *Materials* **2020**, *13*, 1778, https://doi.org/10.3390/ma13071778.
34. Wei, Q.; Luo, G.; Zhang, J.; Jiang, S.; Chen, P.; Shen, Q.; Zhang, L. Designing high entropy alloy-Ceramic eutectic composites of MoNbRe$_{0.5}$TaW$(TiC)_x$ with high compressive strength. *J. Alloys Compd.* **2020**, *818*, 152846, https://doi.org/10.1016/j.jallcom.2019.152846.
35. Xiang, C.; Fu, H.M.; Zhang, Z.M.; Han, E.-H.; Zhang, H.F.; Wang, J.Q.; Hu, G.D. Effect of Cr content on microstructure and properties of $Mo_{0.5}$VNbTiCr_x high-Entropy alloys. *J. Alloys Compd.* **2020**, *818*, 153352, https://doi.org/10.1016/j.jallcom.2019.153352.
36. Edalati, P.; Floriano, R.; Mohammadi, A.; Li, Y.; Zepon, G.; Li, H.-W.; Edalati, K. Reversible room temperature hydrogen storage in high-Entropy alloy TiZrCrMnFeNi. *Scr. Mater.* **2020**, *178*, 387–390, https://doi.org/10.1016/j.scriptamat.2019.12.009.
37. Xiao, D.H.; Zhou, P.F.; Wu, W.Q.; Diao, H.Y.; Gao, M.C.; Song, M.; Liaw, P.K. Microstructure, mechanical and corrosion behaviors of AlCoCuFeNi-(Cr,Ti) high entropy alloys. *Mater. Design* **2017**, *116*, 438–447, https://doi.org/10.1016/j.matdes.2016.12.036.
38. Zhang, C.; Wu, Y.; You, L.; Qiu, W.; Zhang, Y.; Yuan, Y.; Lu, Z.; Song, X. Nanoscale phase separation of TiZrNbTa high entropy alloy induced by hydrogen absorption. *Scr. Mater.* **2020**, *178*, 503–507, https://doi.org/10.1016/j.scriptamat.2019.12.034.
39. Qu, H.Z.; Gong, M.L.; Liu, F.F.; Gao, B.Y.; Bai, J.; Gao, Q.Z.; Li, S. Microstructure, mechanical properties and magnetic properties of FeCoNiCuTiSi_x high-Entropy alloys. *Sci. China Technol. Sci.* **2020**, *63*, 459–466, https://doi.org/10.1007/s11431-019-9549-9.
40. Erdogani, A.; Gök, M.S.; Zeytin, S. Analysis of the high-temperature dry sliding behavior of CoCrFeNi$Ti_{0.5}Al_x$ high-Entropy alloys. *Friction* **2020**, *8*, 198–207, https://doi.org/10.1007/s40544-019-0278-2.

41. Barron, P.J.; Carruthers, A.W.; Fellowes, J.W.; Jones, N.G.; Dawson, H.; Pickering, E.J. Towards V-Based high-Entropy alloys for nuclear fusion applications. *Scr. Mater.* **2020**, *176*, 12–16, https://doi.org/10.1016/j.scriptamat.2019.09.028.
42. Kosorukova, T.A.; Gerstein, G.; Odnosum, V.V.; Koval, Y.N.; Maier, H.J.; Firstov, G.S. Microstructure formation in cast TiZrHfCoNiCu and CoNiCuAlGaIn high entropy shape memory alloys: A comparison. *Materials* **2019**, *12*, 4227, https://doi.org/10.3390/ma12244227.
43. Gurel, S.; Yagci, M.B.; Canadinc, D.; Gerstein, G.; Bal, B.; Maier, H.J. Fracture behavior of novel biomedical Ti-Based high entropy alloys under impact loading. Mater. *Sci. Eng. A* **2021**, *803*, 140456, https://doi.org/10.1016/j.msea.2020.140456.
44. Zeng, X.; Liu, Z.; Wu, G.; Tong, X.; Xiong, Y.; Cheng, X.; Wang, X.; Yamaguchi, T. Microstructure and high-Temperature properties of laser cladded AlCoCrFeNiTi$_{0.5}$ high-Entropy coating on Ti$_6$Al-$_4$V alloy. *Surf. Coat. Technol.* **2021**, *418*, 127243, https://doi.org/10.1016/j.surfcoat.2021.127243.
45. Gu, Z.; Mao, P.; Gou, Y.; Chao, Y.; Xi, S. Microstructure and properties of MgMoNbFeTi$_2$Y$_x$ high entropy alloy coatings by laser cladding. *Surf. Coat. Technol.* **2020**, *402*, 126303, https://doi.org/10.1016/j.surfcoat.2020.126303.
46. Gu, Z.; Xi, S.; Mao, P.; Wang, C. Microstructure and wear behavior of mechanically alloyed powder Al$_x$Mo$_{0.5}$NbFeTiMn$_2$ high entropy alloy coating formed by laser cladding. *Surf. Coat. Technol.* **2020**, *401*, 126244, https://doi.org/10.1016/j.surfcoat.2020.126244.
47. Zhang, Y.; Han, T.; Xiao, M.; Shen, Y. Tribological behavior of diamond reinforced FeNiCoCrTi$_{0.5}$ carbonized highentropy alloy coating. *Surf. Coat. Technol.* **2020**, *401*, 126233, https://doi.org/10.1016/j.surfcoat.2020.126233.
48. Xiang, K.; Chen, L.-Y.; Chai, L.; Guo, N.; Wang, H. Microstructural characteristics and properties of CoCrFeNiNb$_x$ high-Entropy alloy coatings on pure titanium substrate by pulsed laser cladding. *Appl. Surf. Sci.* **2020**, *517*, 146214, https://doi.org/10.1016/j.apsusc.2020.146214.
49. Zhang, Y.; Han, T.; Xiao, M.; Shen, Y. Microstructure and properties of laser-Clad FeNiCoCrTi$_{0.5}$Nb$_{0.5}$ high-Entropy alloy coating, *Mater. Sci. Technol.* **2020**, *36*, 811–818, https://doi.org/10.1080/02670836.2020.1743924.
50. Wang, X.; Liu, Q.; Huang, Y.; Xie, L.; Xu, Q.; Zhao, T. Effect of Ti content on the microstructure and corrosion resistance of CoCrFeNiTi$_x$ high entropy alloys prepared by laser cladding. *Materials* **2020**, *13*, 2209, https://doi.org/10.3390/ma13102209.
51. Li, Y.; Liang, H.; Nie, Q.; Qi, Z.; Deng, D.; Jiang, H.; Cao, Z. Microstructures and wear resistance of CoCrFeNi$_2$V$_{0.5}$Ti$_x$ high-entropy alloy coatings prepared by laser cladding. *Crystals* **2020**, *10*, 352, https://doi.org/10.3390/cryst10050352.
52. Gu, Z.; Xi, S.; Sun, C. Microstructure and properties of laser cladding and CoCr$_{2.5}$FeNi$_2$Ti$_x$ high-Entropy alloy composite coatings. *J. Alloys Compd.* **2020**, *819*, 152986, https://doi.org/10.1016/j.jallcom.2019.152986.
53. Xu, Y.; Li, Z.; Liu, J.; Chen, Y.; Zhang, F.; Wu, L.; Hao, J.; Liu, L. Microstructure evolution and properties of laser cladding CoCrFeNiTiAl$_x$ high-Entropy alloy coatings. *Coatings* **2020**, *10*, 373, https://doi.org/10.3390/coatings10040373.
54. Li, Y.; Shi, Y. Phase assemblage and properties of laser cladded Ti$_x$CrFeCoNiCu high-Entropy alloy coating on aluminum. *Mater. Res. Express* **2020**, *7*, 036519, https://doi.org/10.1088/2053-1591/ab7d0c.
55. Wang, J.; Zhang, B.; Yu, Y.; Zhang, Z.; Zhu, S.; Wang, Z. Ti content effect on microstructure and mechanical properties of plasma-Cladded CoCrFeMnNiTi$_x$ high-Entropy alloy coatings. *Surf. Topogr. Metrol. Prop.* **2020**, *8*, 015004, https://doi.org/10.1088/2051-672X/ab615b.
56. Huber, F.; Bartels, D.; Schmidt, M. In-Situ alloy formation of a WMoTaNbV refractory metal high entropy alloy by laser powder bed fusion (PBF-LB/M). *Materials* **2021**, *14*, 3095, https://doi.org/10.3390/ma14113095.
57. Dada, M.; Popoola, P.; Mathe, N.; Pityana, S.; Adeosun, S.; Aramide, O.; Lengopeng, T. Process optimization of high entropy alloys by laser additive manufacturing. *Eng. Rep.* **2020**, *2*, 12252, https://doi.org/10.1002/eng2.12252.
58. Cui, W.; Li, W.; Chen, W.-T.; Liou, F. Laser Metal Deposition of an AlCoCrFeNiTi$_{0.5}$ High-entropy alloy coating on a Ti6Al4V substrate: Microstructure and oxidation behavior. *Crystals* **2020**, *10*, 638, https://doi.org/10.3390/cryst10080638.
59. Sanin, V.N.; Ikornikov, D.M.; Golosov, O.A.; Andreev, D.E.; Yukhvid, V.I. Centrifugal metallothermic SHS of cast Co–Cr–Fe–Ni–Mn–(X) alloys. *Russ. J. Non Ferr. Metals* **2020**, *61*, 436–445, https://doi.org/10.3103/S1067821220040070.
60. Wang, G.; Sheng, G.; Yu, Q.; Yuan, X.; Sun, J.; Jiao, Y.; Zhang, Y. Investigation of intergranular penetration behavior in CrMnFeCoNi HEA/304 SS dissimilar brazing joints. *Intermetallics* **2020**, *126*, 106940, https://doi.org/10.1016/j.intermet.2020.106940.
61. Wang, G.; Sheng, G.; Sun, J.; Wei, Y.; Gao, X.; Yu, Z.; Yuan, X. Mechanical properties and microstructure evolution of CrMnFeCoNi HEA/304 SS dissimilar brazing joints. *J. Alloys Compd.* **2020**, *829*, 154520, https://doi.org/10.1016/j.jallcom.2020.154520.
62. Straumal, B.; Gust, W.; Molodov, D. Wetting transition on the grain boundaries in Al contacting with Sn-rich melt. *Interface Sci.* **1995**, *3*, 127–132, https://doi.org/10.1007/BF00207014.
63. Straumal, B.B.; Gust, W.; Watanabe, T. Tie lines of the grain boundary wetting phase transition in the Zn-Rich part of the Zn–Sn phase diagram. *Mater. Sci. Forum* **1999**, *294/296*, 411–414, https://doi.org/10.4028/www.scientific.net/MSF.294-296.411.
64. Straumal, A.B.; Yardley, V.A.; Straumal, B.B.; Rodin, A.O. Influence of the grain boundary character on the temperature of transition to complete wetting in Cu–In system. *J. Mater. Sci.* **2015**, *50*, 4762–4771, https://doi.org/10.1007/s10853-015-9025-x.
65. Kogtenkova, O.A.; Straumal, A.B.; Afonikova, N.S.; Mazilkin, A.A.; Kolesnikova, K.I.; Straumal, B.B. Grain boundary wetting phase transitions in peritectic copper—cobalt alloys. *Phys. Sol. State* **2016**, *58*, 743–747, https://doi.org/10.1134/S1063783416040107.
66. Straumal, B.B.; Gornakova, A.S.; Kogtenkova, O.A.; Protasova, S.G.; Sursaeva, V.G.; Baretzky, B. Continuous and discontinuous grain boundary wetting in the Zn–Al system. *Phys. Rev. B* **2008**, *78*, 054202, https://doi.org/10.1103/PhysRevB.78.054202.
67. Gornakova, A.S.; Straumal, B.B.; Tsurekawa, S.; Chang, L.-S.; Nekrasov, A.N. Grain boundary wetting phase transformations in the Zn–Sn and Zn–In systems. *Rev. Adv. Mater. Sci.* **2009**, *21*, 18–26.

68. Straumal, B.; Muschik, T.; Gust, W.; Predel, B. The wetting transition in high and low energy grain boundaries in the Cu(In) system. *Acta Metall. Mater.* **1992**, *40*, 939–945, https://doi.org/10.1016/0956-7151(92)90070-U.
69. Maksimova, E.L.; Shvindlerman, L.S.; Straumal, B.B. Transformation of Σ17 special tilt boundaries to general boundaries in tin. *Acta Metall. Mater.* **1988**, *36*, 1573–1583, https://doi.org/10.1016/0001-6160(88)90225-8.
70. Ernst, F.; Finnis, M.W.; Koch, A.; Schmidt, C.; Straumal, B.; Gust, W. Structure and energy of twin boundaries in copper. *Z. Metallk.* **1996**, *87*, 911–922.
71. Straumal, B.B.; Baretzky, B. Grain boundary phase transitions and their influence on properties of polycrystals. *Interf. Sci.* **2004**, *12*, 147–155, https://doi.org/10.1023/B:INTS.0000028645.30358.f5.
72. Straumal, A.B.; Bokstein, B.S.; Petelin, A.L.; Straumal, B.B.; Baretzky, B.; Rodin, A.O.; Nekrasov, A.N. Apparently complete grain boundary wetting in Cu–In alloys. *J. Mater. Sci.* **2012**, *47*, 8336–8343, https://doi.org/10.1007/s10853-012-6773-8.
73. Noskovich, O.I.; Rabkin, E.I.; Semenov, V.N.; Straumal, B.B.; Shvindlerman, L.S. Wetting and premelting phase transitions in 38° [100] tilt grain boundaries in (Fe–12 at.% Si) Zn alloy in the vicinity of the A2–B2 bulk ordering in Fe–12 at. % Si alloy. *Acta Metall. Mater.* **1991**, *39*, 3091–3098, https://doi.org/10.1016/0956-7151(91)90042-Y.
74. Straumal, B.B.; Noskovich, O.I.; Semenov, V.N.; Shvindlerman, L.S.; Gust, W.; Predel, B. Premelting transition on 38°<100> tilt grain boundaries in (Fe–10at.%Si)–Zn alloys. *Acta Metall. Mater.* **1992**, *40*, 795–801, https://doi.org/10.1016/0956-7151(92)90021-6.
75. Rabkin, E.I.; Shvindlerman, L.S.; Straumal, B.B. Grain boundaries: Phase transitions and critical phenomena. *Int. J. Mod. Phys. B* **1991**, *5*, 2989–3028, https://doi.org/10.1142/S0217979291001176.
76. Straumal, B.B.; Zięba, P.; Gust, W. Grain boundary phase transitions and phase diagrams. *Intern. J. Inorgan. Mater.* **2001**, *3*, 1113–1115, https://doi.org/10.1016/S1466-6049(01)00108-8.
77. Straumal, B.B.; Mazilkin, A.A.; Baretzky, B. Grain boundary complexions and pseudopartial wetting. *Curr. Opin. Sol. State Mater. Sci.* **2016**, *20*, 247–256, https://doi.org/10.1016/j.cossms.2016.05.006.
78. Straumal, B.B.; Kogtenkova, O.A.; Straumal, A.B.; Baretzky, B. Grain boundary wetting-related phase transformations in Al and Cu-based alloys. *Lett. Mater.* **2018**, *8*, 364–371, https://doi.org/10.22226/2410-3535-2018-3-364-371.